Microchemical Journal 218 (2025) 115559

Contents lists available at ScienceDirect

Microchemical Journal

journal homepage: www.elsevier.com/locate/microc

Analytical strategies to evaluate the in-depth degradation processes in protein-based heritage substrates exposed to ion beam techniques

Mingchi Ma [a], Zelan Li [a], Giorgia Sciutto [a], Martina Zangari [b], Tommaso Salzillo [b], Elisabetta Venuti [b], Zita Szikszai [c], Boglárka Döncző [c], Silvia Prati [a,*]

[a] Microchemical and Microscopy Art Diagnostic Laboratory, Department of Chemistry, University of Bologna, Department of Chemistry-Ravenna Campus, Via Guaccimanni 42, 48121 Ravenna, Italy
[b] Molecular Spectroscopy Group, Department of Industrial Chemistry, University of Bologna, Via Gobetti 85, 40129 Bologna, Italy
[c] HUN-REN Institute for Nuclear Research (ATOMKI), Bem tér 18/c, H-4026 Debrecen, Hungary

ARTICLE INFO

Keywords:
In depth damage detection
FTIR
NIR
Parchment
Silk

ABSTRACT

This study is aimed at proposing an analytical protocol to study the in-depth effects of ion beams technique on protein-based heritage materials such as parchment and silk, exploiting the penetration of Near-Infrared (NIR) and of confocal micro-Raman (μ-Raman) spectroscopy. The objective is to verify if the two techniques are suitable to identify the main chemical modifications induced by varying proton beam fluences. As a proof of concept a series of parchment and silk samples were exposed to varying doses of proton beam irradiation (from 0.125, up to 20 μC/cm^2, provided by ATOMKI) and then submitted to micro-FTIR spectroscopy (μ-FTIR) in mapping mode (7000–675 cm^{-1}) and μ-Raman spectroscopy. By collecting three-dimensional dataset of irradiated versus unirradiated regions, the extent of degradation in response to different levels of proton beam dosage was identified employing a multivariate statistical approach based on principal component analysis (PCA). PCA proved efficient in reducing the dimensionality of the large spectroscopic datasets and in highlighting the most relevant spectral features responsible for the irradiation-induced modifications across the near-infrared and mid-infrared regions. Results from this study indicate that μ-FTIR mapping in the NIR spectral region enables intuitive identification of modifications induced by proton beam fluence range from 0.5 to 20 μC/cm^2 for parchment and 1 to 20 μC/cm^2 for silk. In addition, the μ-Raman analysis revealed that deeper layers of the samples are susceptible to damage at doses as low as 0.125 μC/cm^2. This finding provides valuable insights into the vulnerability of protein-based materials when subjected to ion beam analysis (IBA), contributing to the determination of safe analytical conditions for performing such analyses.

1. Introduction

Ion Beam Analysis (IBA) is recognized for its unique capabilities in the non-destructive elemental analysis of cultural heritage artifacts. External beam IBA techniques, such as Particle Induced X-ray Emission (PIXE), Particle Induced Gamma-ray Emission (PIGE), and Rutherford or Elastic Backscattering Spectrometry (RBS/EBS), offer complementary information, allowing the detection of both light and heavy elements [1]. However, a key limitation of IBA concerns radiation damage, particularly in organic-based materials.

Recent studies have increasingly focused on evaluating its effects on protein-based materials like parchment and silk [2,3]. High-dose exposure to ion beams can lead to collagen degradation through denaturation, hydrolysis, and oxidation processes [2–4]. These chemical changes can alter the material's chemical structure and cause visible damage such as yellowing or darkening of the analyzed area. Moreover, the internal structure may also be affected due to the Bragg peak phenomenon [5], where protons lose energy gradually as they traverse a medium, with a dramatic energy deposition occurring near the end of their path. This localized energy transfer can cause substantial internal damage, while the dose sharply declines beyond the Bragg peak. This property is utilized in therapeutic applications to enable precise energy deposition, as exemplified by proton therapy for cancer treatment, which permits the delivery of high radiation doses to tumours while sparing adjacent healthy tissues [6].

On the other hand, the possible occurrence of in-depth damage on

* Corresponding author.
E-mail address: s.prati@unibo.it (S. Prati).

https://doi.org/10.1016/j.microc.2025.115559
Received 15 July 2025; Received in revised form 16 September 2025; Accepted 26 September 2025
Available online 28 September 2025

cultural heritage artefact analyzed with IBA creates concerns, especially when fragile substrates are analyzed such as parchment and silk.

In the specific case of PIXE applied to paintings, a safety threshold of 1 μC/cm^2 has been established for organic binders, known to be among the most sensitive components in paint layers [7]. For painted parchment, Müller et al. determined a lower safety limit of 0.5 μC/cm^2 for 2.3 MeV protons, using synchrotron-based two-dimensional Fourier Transform Infrared (Sy-2D-FTIR) mapping. Exceeding this threshold (e.g., above 4 μC/cm^2) led to observable degradation, such as cavity formation and collagen fiber denaturation extending to depths of approximately 100 μm.

Subsequent work by Csepregi et al. [3] employed different techniques to study parchment exposed to different doses. Fourier Transform Infrared Spectroscopy in Attenuated Total Reflectance (FTIR-ATR) mode were capable to identify degradation features in samples exposed to 2.3 MeV, 5–10 μC/cm^2. While changes were less apparent below this threshold, complementary imaging via Optical Coherence Tomography, performed after sample immersion, revealed crater formation and confirmed a proton penetration depth of around 100 μm, even at doses as low as 1 μC/cm^2.

Numerous studies proposed FTIR spectroscopy in the mid-infrared (MIR) range to evaluate parchment aging [2–4]. Collagen, the primary component of parchment, exhibits characteristic amide I, II, and III bands in FTIR spectra. Degradation processes such as denaturation, hydrolysis, and oxidation manifest through specific spectral shifts and intensity changes. For instance, collagen denaturation is evidenced by shifts in the amide I band and amide II respectively to higher and to lower wavenumbers, increasing the distance between them [8]. Hydrolysis leads to scission of the polypeptide chains, altering the amide I/amide II intensity ratio, while oxidation (e.g., from light and pollutants) can generate carbonyl groups, seen as an enlargement of the amide I band area [4].

Similar to FTIR, the Raman spectrum of parchment is characterized by the distinctive vibrational features of collagen [9]. Prominently, amide I and III bands appear, while the amide II band is usually quite weak. A band near 1450 cm^{-1} corresponds to aliphatic C—H bending vibrations, and the intensity ratio between amide I and this band has been proposed as a marker of collagen degradation [10,11]. In the 1100–900 cm^{-1} region, several bands appear that are attributed to the C—C stretching of both proline and hydroxyproline rings and of protein backbone [12]. Changes across the fingerprint region are identified, which are related to aging processes [13]. In particular, after 24 h of UV irradiation, Reina et al. [14] found that the Raman spectrum of parchment displayed significant broadening between 800 and 1200 cm^{-1}, with bands associated with C—C vibrations becoming less defined and accompanied by the occurrence of a new feature at 1084 cm^{-1}, likely attributable to disordered C—C stretching modes from random coil configurations.

Silk, composed primarily of fibroin and sericin, is also highly susceptible to degradation caused by humidity, UV light, and pollutants. These factors can induce oxidative chain breaks, reducing mechanical performance and altering the fiber's secondary structure [15,16]. In MIR spectra, oxidation in silk is typically identified by changes in the carbonyl region (1775–1700 cm^{-1}), associated with β-turns in the β-sheet structure [17]. However, unlike parchment, silk does not show significant amide I variation with aging. Instead, the crystalline index of amide III serves as a more sensitive marker for structural changes [16]. Key Raman bands of silk fibroin provide information about secondary structure and local environment, and therefore degradation processes [18,19]. The tyrosine doublet at 830 and 850 cm^{-1} reflects local interactions involving tyrosine residues. The structured amide III region (1300–1200 cm^{-1}) is sensitive to backbone conformation and β-sheet orientation. The amide I band, typically centered around 1670–1665 cm^{-1}, also serves as a marker for β-sheet content. While prior studies have mainly focused on the amide I and tyrosine bands, the amide III region also provides valuable conformational information [18].

FTIR-ATR provides surface information, with a penetration depth of about 1.66 μm at 1000 cm^{-1} for parchment (Csepregi et al. [3]), and requires intimate contact with the artefact. Based on the evanescent-wave penetration depth equation reported by Rosi et al. [20], the use of a Ge crystal (n ≈ 4) in the range 4000–675 cm^{-1} confines measurements to the near-surface region and does not capture deeper modifications induced by proton beam irradiation. Moreover, Badillo-Sanchez et al. [21] suggested that the mechanical pressure exerted by the ATR crystal can alter silk fibers, potentially masking spectral differences between pristine and aged samples. Since ion-beam damage (PIXE) can extend tens to hundreds of microns beneath the surface, techniques with greater probing depth are required.

Padalkar and Pleshko [22] demonstrated that in collagen-rich tissues such as cartilage, NIR penetration depths of 1–3 mm are achievable. Since parchment is likewise predominantly composed of collagen, NIR spectroscopy is expected to probe depths well beyond 100 μm, where Csepregi et al. [3] previously observed ion-beam damage with 2.3 MeV protons.

To identify a suitable analytical approach capable to sample in depth degradation processes due to ion beam exposure [2,3], this study examined a new set of goatskin samples and silk samples that have undergone proton beam irradiation using μ-FTIR mapping, isolating MIR (4000–675 cm^{-1}) and NIR (7000–4000 cm^{-1}) regions. Principal Component Analysis (PCA) and brushing techniques [23] revealed that NIR spectroscopy effectively detects subsurface proton-induced modifications not evident in surface analyses.

In parallel, confocal μ-Raman spectroscopy was employed to exploit its probing depth determined by its axial resolution [24], which reflects the depth from which the Raman signal is effectively collected and spatially resolved. The axial resolution is, in turn, a function of the setup optics and of the excitation wavelength, as well as of the refraction index of the probed medium and its scattering and absorption properties. Therefore, the knowledge of the axial resolution allows to assess the spatial extent of modifications within the samples.

In this work, lower-energy protons were used compared to previous studies [2,3], producing damage confined to the first 50–60 μm. This experimental choice allowed us to test whether the in-depth penetration of NIR and μ-Raman spectroscopy, which extends beyond this thickness, is suitable for detecting the expected modifications within the irradiated volume.

Overall, the results highlight the enhanced sensitivity and suitability of NIR and μ-Raman spectroscopy for monitoring ion-beam-induced damage in fragile organic materials such as parchment and silk, supporting their application in the study of cultural heritage affected by Ion Beam Analysis (IBA).

2. Materials and methods

2.1. Parchment and silk samples

Commercially available goatskin parchment produced traditionally in Turkey and silk samples were exposed to proton beam irradiation at the external beamline of the Tandetron accelerator of HUN-REN ATOMKI [25,26] with protons produced at 2.0 MeV that, mainly as a result of Coulomb interactions with electrons, hit the sample with an energy of 1.73 MeV.

The beam spot was 2 mm × 2 mm, and the samples were scanned in front of the beam, covering an area of 8 mm × 9 mm (Fig. S1). Different fluences, corresponding to the amount of charge, deposited on a unit area of the sample surface [27], were employed from 0.125 to 20 μC/cm^2 with the current ranging from 1 nA (lowest fluence) to 9 nA (for the other fluences), resulting in noticeable discoloration (yellowing) on parchment surface associated with the highest dose exposure. The range of applied fluences includes conditions commonly employed for IBA purposes [28]. The highest fluence condition (20 μC/cm^2) has been included to assess more extreme conditions. The deposited charge is

expected to be homogeneous on the surface, perpendicular to the beam axis, except from the edges of the irradiation. Details regarding the beam fluences for the analyzed samples and the irradiation scheme are outlined in Table 1.

2.2. Stereo microscopy

All samples were documented prior to FTIR analysis using a Leica MZ6 stereo microscope equipped with Tungsten lamp, and a Canon® Power Shot 550 digital camera mounted on the ocular. The irradiation spots were positioned on the lighter and smoother side (for the parchment), measuring approximately 8 × 8 mm^2. This method can utilize the surface discoloration observed in highly irradiated samples to locate areas for the following μ-FTIR analyses.

2.3. Micro-FTIR point analyses and mapping

An Infrared Microscope Thermo Scientific Nicolet (Thermo Fisher Scientific, Waltham, MA, USA) iN™10MX spectrometer cooled by liquid nitrogen, equipped with a X–Y–Z motorized stage, was used in ER mode to record the spectra in the range 7000–675 cm^{-1}, with a spectral resolution of 8 cm^{-1}. The optical aperture was 300 × 300 μm^2. Background was collected from a 200 nm gold-coated slide. Point analyses were performed on both the irradiated and unirradiated areas of parchment P20 and silk S20 to compare degradation spectral features. Maps were acquired by attaching two sides of parchment and silk samples with adhesive tape onto a gold coated glass slide, ensuring the tissue was placed flat to maintain a planar surface. The analyses were carried out on the regions around the midsection of P0.125 to P20 and S0.125 to S20, which also included the unirradiated areas, as indicated by a red rectangle (Fig. S4a).

2.4. Data-processing methods

The preliminary data-handling of the spectral datasets obtained by μ-FTIR mapping was carried out using the specialized software OMNIC™ and OMNIC Picta™ (Thermo Fisher Scientific, Waltham, MA, USA), and data-processing was performed by MATLAB (R2023b, The MathWorks, Inc.). During data pre-processing, MIR (4000–675 cm^{-1}) and NIR (7000–4000 cm^{-1}) were treated with individual methods. The MIR and the NIR components were elaborated separately using PCA. Standard Normal Variate (SNV) correction followed by quadratic detrending was effectively applied to compensate for baseline shifts and slope variations [29,30]. Savitzky-Golay (SG) first derivative to further enhanced spectral features. The NIR region between 7000 and 5200 cm^{-1}, predominantly reflecting water content, was excluded due to low Signal-to-Noise Ratio (SNR). For silk, a tailored approach using SG smoothing and second-derivative transformation was employed to address unique scattering and baseline drift challenges in both MIR and NIR ranges [31,32].

Based on the PCA results, a brushing workflow (Fig. 1) was applied for an in-depth exploratory analysis. This approach enabled the interactive selection of pixel clusters directly from the PCA score map (Fig. 1a), which were then analyzed in the corresponding score plot (Fig. 1b) to distinguish chemically distinct regions. The associated spectral profiles (Fig. 1c) and PC loadings (Fig. 1d) were subsequently examined to correlate specific spectral variations with chemical changes induced by proton beam irradiation. This method effectively revealed irradiation-driven chemical transformations and allowed the characterization of the distinct spectral features of the two materials.

Average spectra for each region were selected by brushing on the score maps, the corresponding spectra were extracted from the original dataset and then pre-processed to facilitate the interpretation of spectral features and their correlation with the effects of proton beam irradiation. For the parchment samples, the raw dataset was treated with SNV and detrending, whereas for the silk samples, an auto baseline correction preceded SNV. PCA score maps show how pixels are grouped based on spectral similarity, allowing the identification of chemically distinct regions, such as irradiated and non-irradiated areas. The loading profiles indicate which wavenumbers (variables) contribute mostly to this separation. Wavenumbers with positive loadings are more strongly associated with pixels having positive scores, whereas wavenumbers with negative loadings are more strongly associated with pixels having negative scores. Thus, by combining information from score maps and loadings, it is possible to verify wether it is possible to distinguish irradiated and non-irradiated regions and to identify the spectral features, which may mainly drive the differentiation.

Table 1
Fluences applied to parchment (P) and silk (S) samples.

Sample name	Charge per unit area (μC/cm^2)
P20/S20	20
P10/S10	10
P4/S4	4
P2/S2	2
P1/S1	1
P0.5/S0.5	0.5
P0.25/S0.25	0.25
P0.125/S0.125	0.125

2.5. Confocal micro-Raman (μ-Raman) spectroscopy

Raman spectra were acquired using a confocal Raman microscope (Xplora Plus, Horiba) equipped with a 785 nm diode laser as the excitation source. The laser was operated at 25 % of its nominal 100 mW power to minimize the risk of thermal damage of the sample. The spectrometer is equipped with edge filters enabling the scattering collection down to 50 cm^{-1} from the Rayleigh line. All data presented in this work were recorded using the 5× objective, which was selected to access the maximum possible penetration depth under the excitation at 785 nm in order to observe in depth damages in the range 50–60 μm as explained above. This configuration was purposefully adopted to assess structural alterations induced by proton beam irradiation at the greatest depth accessible by the system. In a confocal setup, the effective sampling depth depends on the excitation wavelength λ, the numerical aperture NA of the objective, and the pinhole diameter. With the fixed pinhole aperture applied for these measurements, axial resolution is governed only by the optical characteristics of the objective, i.e. NA and working distance, which also define the confocal volume and collection efficiency. Following Chalmers et al. (2002) [24], the theoretical axial resolution Δz is calculated with Eq. (1) and the penetration depth can be thus estimated. For the 5× objective, the maximum penetration depth thus reaches approximately 100 μm. Even though actual depths may vary depending on the sample's scattering and absorption properties, it is reasonable to assume that, in not strongly absorbing samples, the penetration depth is approximately equal to the axial resolution, as both are primarily governed by the optical characteristics of the confocal setup [33].

$$\Delta z \geq \pm \frac{4.4 n \lambda}{2\pi (NA)^2} \quad (1)$$

For each sample, both of parchment and silk, irradiated with varying proton beam doses as described in Section 2.1, five spectra were acquired and averaged. Each spectrum, focused on the 800–2000 cm^{-1} range, resulted from a 50 s accumulation, chosen to accurately determine Raman peak positions and improve the signal to noise ratio. Spectra were collected from at least three distinct points within the selected micro-area for each experimental condition. Data processing, including baseline correction and peak assignment, was performed using OriginPro 2024.

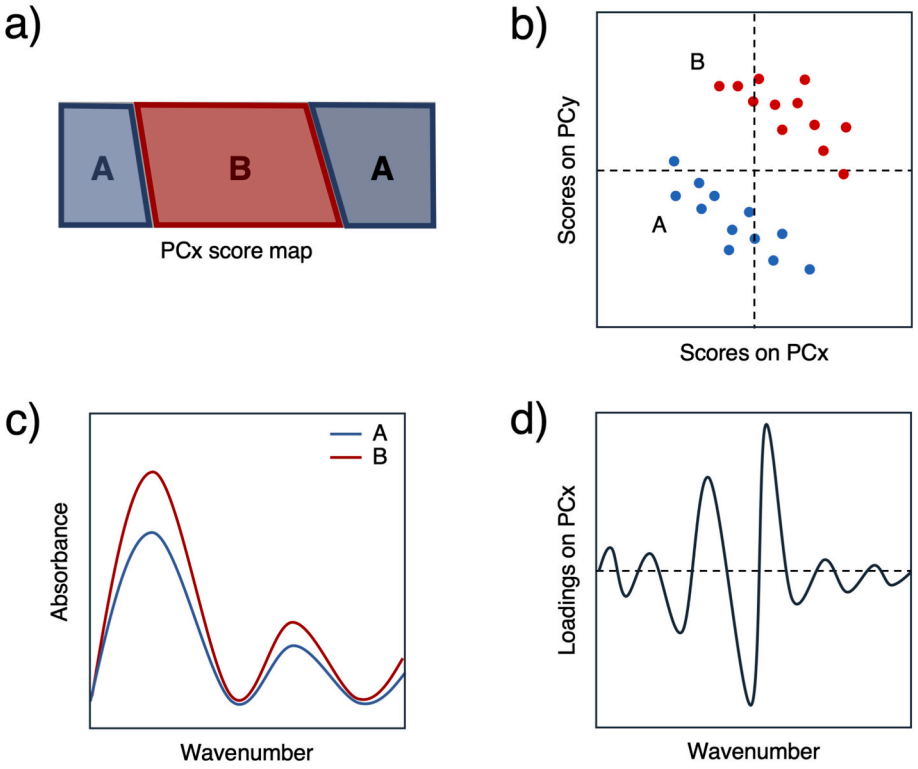

Fig. 1. Workflow for PCA brushing: (a) selection of pixels based on the PCx score maps; (b) identification of cluster in the PCx-PCy score plots; (c) and (d) evaluation of the average spectra and of the loading profiles.

3. Results

Parchment and silk samples were exposed to proton beam irradiation with protons that hit the sample with an energy of 1.73 MeV, a value that is within the typical energy range for ion beam analysis (MeV range), although somewhat lower than the energy used in previous studies [2,3]. The selected conditions allow to reduce the penetration depth of the particles into the material with the aim to verify whether techniques with can penetrate up to hundreds of microns can be suitable to detect changes which occur below the first 100 μm [28]. The in depth-dose profile, is not uniform due to the Bragg peak phenomenon [34]. Consequently, damage is expected to be more pronounced near the end of the proton's path. In particular, since the penetration depth of the protons depends just on the energy of the particles and on the type of material, for parchment, the projected penetration depth can be estimated to be in the order of 50–60 μm. For silk, the woven microstructure and porosity introduce local density/voids that can disturb the effective path length, therefore range values should be interpreted with greater caution than for parchment.

Parchment and silk samples exposed to various irradiation conditions were analyzed using μ-FTIR microscopy in external reflection (ER) mode, acquiring spectral maps of areas that included both irradiated and non-irradiated zones in the MIR and the NIR range. The two regions were then elaborated separately exploiting the different penetration depth in the two regions of the infrared range and the data were processed using PCA. It is important to note that spectra acquired in ER mode appear distorted in the MIR range compared to those obtained using ATR or transmission modes. These distortions arise from the combined effects of specular reflection (Rs) and volume reflection (Rv) contributing to the total reflected signal.

Rs can introduce spectral distortions such as derivative-like features and band inversion (Reststrahlen effect), making mathematical correction difficult when these effects coexist. In such cases, signal identification will rely on pseudobands, apparent features not linked to true vibrational transitions but to optical artifacts. In contrast, as light is scattered back from within the bulk, Rv enhances weak bands, especially overtones and combinations in the NIR which are not distorted. Since silk and parchment have different morphology, the relative contributions of Rs and Rv will be different such as their characteristic spectral features [35].

Fig. S2 show ER spectra collected from untreated areas of pristine parchment and silk, while Table S1 summarizes the band assignments based on the observed spectral distortions.

In ER-FTIR spectra of parchment (Fig. 1a), the Amide I and Amide II bands display typical derivative-like distortions, with inflection points located at approximately 1665 cm^{-1} (Amide I) and 1555 cm^{-1} (Amide II). The pseudo bands employed for their detection correspond approximately to 1690 cm^{-1} and 1580 cm^{-1} as observed in reflection spectra acquired on collagen based materials [36].

In the case of silk, although the macroscopic surface may appear uneven, individual fibers are microscopically glossy. This intrinsic glossiness enhances specular reflection, contributing to prominent spectral distortions in ER mode, especially the appearance of inverted bands in the amide region. As shown in Table S1, the most informative pseudo absorbance bands for identifying Amide I and Amide II in silk are located around 1705 cm^{-1}, 1680 cm^{-1}, and 1565 cm^{-1} [35].

In the NIR range overtones and combination bands are reported in Table S1.

PCA analyses reported in the following paragraphs were performed after the selected pre-treatments, taking into consideration the different morphology of the two materials which impact the baseline of the spectra, especially in the NIR region. In particular, silk tends to be smooth and glossy, resulting in more specular reflection, whereas parchment is rough and fibrous, leading to more diffuse scattering exhibiting greater baseline drift compared to the silk.

3.1. Parchment degradation

Calf parchment samples exposed to various proton irradiation doses with protons of 2.4 MeV were analyzed in a previous paper using ATR-FTIR [3] showing spectral changes induced by proton beams especially at higher doses (5–10 μC/cm^2). A shift of the amide II peak from 1534 to 1540 cm^{-1} to 1522 cm^{-1} was noted, suggesting increased molecular disorder and collagen denaturation [4].

The application of PCA to the spectra acquired on the new set of goat skin samples in the MIR range revealed more information than previously reported [2,3], even if they were treated with proton at lower energy. Indeed the irradiated i regions can be distinguished from the unirradiated ones at doses as low as 2 μC/cm^2 (Fig. S3a).

As an exmaple, the PC1 score map for sample P20 (Fig. S4a) clearly differentiates treated and untreated zones. Based on PC1 values on the PC1 score map, it is possible by brushing to identify three clusters as confirmed by the PC1–PC2 score plot (Fig. S4b). Cluster A corresponds to the unexposed region and its average spectra reported in log1/R is characterized by the typical spectral features of pristine parchment, including the pseudo bands at 1700–1600 cm^{-1} (amide I) and 1580–1510 cm^{-1} (amide II), as reported in Table S1 (Supplementary).

The average spectrum of Cluster B (treated area, Fig. S4c) shows spectral changes associated with degradation [2,4]:

1. A shift of the amide I pseudoband to higher wavenumbers and an increased separation between amide I and II pseudobands, characteristic of collagen denaturation.
2. Altered amide I/amide II intensity ratio, indicating hydrolysis of collagen polypeptide chains.
3. Broadening of the amide I pseudoband, possibly linked to oxidation processes.

A third separation can be done in the frame of cluster B based on the PC1 values identifing a third group of pixels (cluster C, Fig. S4a). The average spectra, while similar to cluster B, exhibit an additional enlargement of the amide I band and a shift of the amide II towards lower wavenumbers ascribable to denaturation processes [4]. These changes align with the more pronounced yellowing observed in the corresponding area under visible light, as shown by the spatial correlation in Fig. S4a.

Notable variations in the loadings are observed in the 1750–1500 cm^{-1} range, corresponding to the Amide I and Amide II bands (after first derivative correction). In particular, the positive loadings at 1566 cm^{-1} reflects a change in the shape of the Amide II band, while the negative loading at 1704 cm^{-1} is associated with a shift in the Amide *I* band when comparing treated and untreated areas. These changes in the Amide I region also appear to contribute to the slight separation observed between clusters B and C.

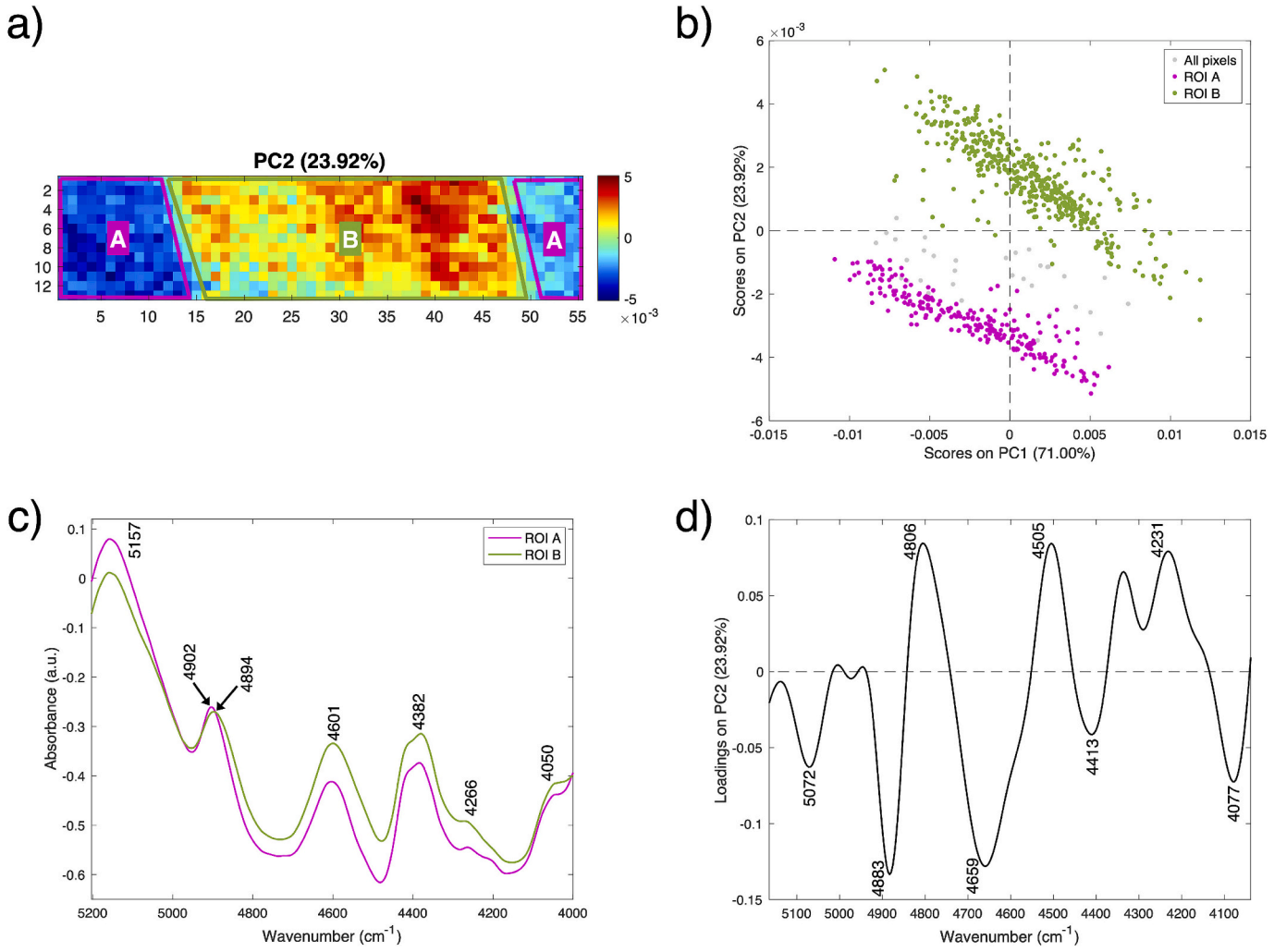

Fig. 2. PCA brushing results of P20 on PC2 score map with a focus on selected NIR region (5200–4000 cm^{-1}). (a) PC2 score map brushing areas; (b) highlighted scores in PCA score plot of two clusters: unirradiated area (A); irradiated area (B); (c) corresponding average spectra with (d) PC2 loading profile from the first derivative PCA model.

Similar spectral features were observed in samples exposed to 10, 4 and 2 μC/cm^2 (samples P10-P2), while at lower doses, MIR spectra could not clearly differentiate treated from untreated zones (Fig. S7–S9).

In the NIR region, PCA of the spectral maps allowed for the differentiation of treated and untreated zones even in the sample irradiated with only 0.5 μC/cm^2 (P0.5), as shown in Fig. S3b.

The PC2 score map for sample P20 (Fig. 2a) allow to distinguish two clusters which correspond to two separate groups in the PC1–PC2 plot. (See Fig. 2b.)

The average spectrum for cluster A (untreated region) shows significant differences in the relative intensities of water-associated bands, particularly the water-related signal at 5157 cm^{-1} [8] with respect to the band around 4601 cm^{-1} (linked to the combination band of amide II and first overtone of carbonyl stretching [37]), and of the broad bands in the 4464–4049 cm^{-1} range, attributed to CH stretching and bending combination modes with respect to the untreated areas [38]. Moreover, a change in the shape of the band at about 4902 cm^{-1} ascribable to the combination band of amide II and first overtone of carbonyl stretching can be observed [37]. The loading plot, derived from spectra processed with a first derivative correction, indicates that the shape of this band significantly influences the separation of the clusters. In particular, the broadening of the amide I band and the shift between the amide I and amide II bands, as previously observed in the MIR range, likely contribute to the variations observed in this spectral region.

These distinctions remain evident in for samples P10, P4, P2, and P1 (Figs. S10–S13). Although cluster separation is less pronounced in the lower-dose samples, brushing the PC1 or PC2 score maps still yields average spectra that confirm the same degradation features.

In sample P0.5 the separation appears less pronounced and the analyses of loadings is not completely clear (Fig. S14).

Interestingly, exploiting just the MIR region it was not possible to distinguish the samples exposed to lower dose, emphasizing the role of the Bragg peak, which causes greater energy deposition, and thus more damage, within the internal layers of the sample rather than on its surface. Consequently, the radiation-induced changes observed in P2, P1 are not detectable under stereomicroscopy or through surface-level FTIR analysis in the mid-IR range.

On the other hand, it is interesting to note that in the P20 treated samples just the superficial information allowed to distinguish cluster C from cluster B which appear not distinguishable considering the NIR range.

To complement the findings of IR spectroscopy techniques, μ-Raman spectroscopy was applied to the parchment samples to verify the depth of the sample damage, depending on the doses. As described in Section 2.5, spectra were recorded using the 5× objective, chosen to achieve the maximum possible penetration depth of 100 μm under the excitation source of 785 nm. The fingerprint region between 800 and 1200 cm^{-1} displays the most pronounced effects of proton-induced damage. As Reina et al. have demonstrated, the exposure of parchment to UV radiation causes the bands of the fingerprint region to become broader and/or decrease dramatically in intensity, indicating a protein structural modification [14]. For the parchment samples exposed to the proton beam, no significant changes were observed in the fingerprint region when comparing the untreated P0 sample with those irradiated at doses up to 4 μC/cm^2. At higher doses, i.e. above 10 μC/cm^2, some bands start to exhibit a marked reduction in intensity and/or broadening, indicating progressive structural degradation. Although the measured signal at each specific micrometric spot showed some dependence on accumulation time, and increasing the SNR required careful control to avoid fluorescence emission and/or excitation-induced damage, the results were consistently uniform over all measured spots. These observations are consistent with those reported by Müller et al. (2022), who found that beam fluences exceeding 4 μC/cm^2 led to substantial modifications in the spectral feature over this range [2].

However, rather than the absence of broad spectral degradation at low doses, a specific marker of early damage, namely, the appearance of a new vibrational band at approximately 1087 cm^{-1} characterizes the Raman spectra (Fig. 3). This band, not observed in the pristine sample, is attributed to C—C random coil vibrations and should be indicative of C═C double bond breakage induced by the proton beam irradiation [14,39,40]. Indeed, a signal corresponding to this band is detected starting from the 0.125 μC/cm^2 fluence, thus suggesting a damage at the beam penetration depth of at least 100 μm, despite the level of noise of this acquisition. As expected, the relative intensity of the 1087 cm^{-1} band varies across the sample, but when present it provides compelling evidence of collagen structural modification at the site of the proton beam exposure.

Unlike what was found in the IR analyses, no clear evidence of the degradation of the secondary structure of the parchment's protein content by proton beam treatment was observed in the Raman spectra under the present experimental conditions. This is supported by the consistent frequency of the Amide I band (1670 cm^{-1}, CO stretching) across all doses and sample layer and the constant intensity ratio between the Amide I and C—H bending (1450 cm^{-1}) bands, whose is considered a marker for collagen degradation [41]. Similarly, the Amide III (1243 cm^{-1}), attributed to CN stretching, appear unchanged in all test conditions. The Amide II band, expected around 1550 cm^{-1} is not detectable. The lack of clear Raman information of collagen degradation in the amide bands of treated parchment may arise from using the 785 nm laser excitation source. While this wavelength effectively suppressed the sample fluorescence, it turned out not to be optimal for detecting the subtle conformational changes identified by NIR and mid-IR spectroscopies. Thus, IR spectroscopy appears to stand as the gold standard in the analyses of amide I and III bands, due to its higher intrinsic sensitivity to peptide backbone vibrations and its widespread use in quantitative curve fitting for secondary structure assessment [42].

3.2. Silk degradation

Silk samples appear to be more stable than parchment, showing only slight visual changes in the treated areas even at high radiation doses (Fig. S5c).

Using MIR spectroscopy combined with PCA, subtle differences

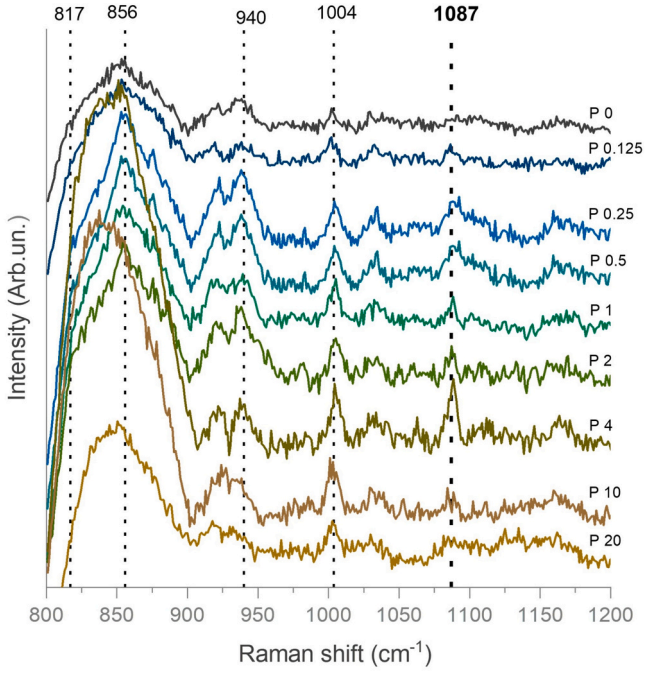

Fig. 3. μ-Raman spectra of proton-irradiated parchment samples. Samples are labeled as in Table 1. The effects of the proton beam were analyzed at the penetration depth of ≈ 100 μm.

between treated and untreated areas are detectable up to sample S4 (Fig. S5a).

In sample S20 (Fig. S6), brushing based on PC2 values in the PC2 score map enables a clear distinction between treated and untreated regions. The average spectra highlight differences in the shape of the amide I and amide II bands (Fig. S6c). The slight broadening of the Amide I band, is possibly due to oxidation processes. Additionally, changes around 1566 cm^{-1} likely correspond to alterations in the shape of the amide II band. The PC2 loading profile (Fig. S6e) further supports the interpretation that variations in both the shape and position of the amide I and II bands are key factors driving the separation between treated and untreated areas based on PC2 values. Similar trends are observed in samples S10 and S4 (Figs. S15–S16), although the separation between treated and untreated areas is less pronounced.

In the NIR region (Fig. S5b), treated and untreated areas can be distinguished through brushing, up to sample S1. The average spectra of the two clusters isolated from sample S20 (Fig. 4), reveal spectral differences in the regions corresponding to the bands at 4860, 4625, and 4536 cm^{-1} ascribable to combination bands of amide I, amide II, amide A, and amide B, as detailed in Table S1. A certain difference can be visible also in in samples S10, S4, S2, and S1 (Figs. S15–S20), where brushing permits a separation, even if less evident.

To assess whether the higher resilience of silk compared to parchment, as revealed by IR techniques, was consistent across different sample depths, the materials were also analyzed using μ-Raman spectroscopy. Fig. 5 displays the spectra acquired from each sample using the 5× objective with a penetration depth of 100 μm. Amide I and Amide III band appear constantly at 1665 and 1233 cm^{-1}, respectively, indicating that both untreated and treated samples adopt predominantly a β-sheet conformation [19,43] in all the tested conditions. It is worth noting that native fibroin, the primary protein in silk, predominantly adopts random coil and α-helix conformations before being spun or processed [19,44]. After extraction from the silkworm cocoon and subsequent reprocessing for the fabrication of silk fibers, molecular alignment occurs, especially under higher drawing ratios, which results in the formation of ordered β-sheet structures [19]. Zheng et al. (1989) identified the band at 1085 cm^{-1} as highly sensitive these structures, and proposed it as a marker of protein conformation [19]. The presence of this band in the spectrum of sample S0 under the reference conditions suggests that the protein is already predominantly in a β-sheet conformation, with no further detectable changes observed in the Raman spectra upon irradiation at all depths. A tentative PCA analysis, comparing the sets of silk samples irradiated with different proton beam fluences further supported this interpretation, indicating that no significant conformational differences are detectable under the tested conditions.

Interestingly, Shao et al. [45] have reported that the photosensitive amino acids such as tryptophan, tyrosine, and phenylalanine are key markers of silk structural changes induced by UV/ozone irradiation. In

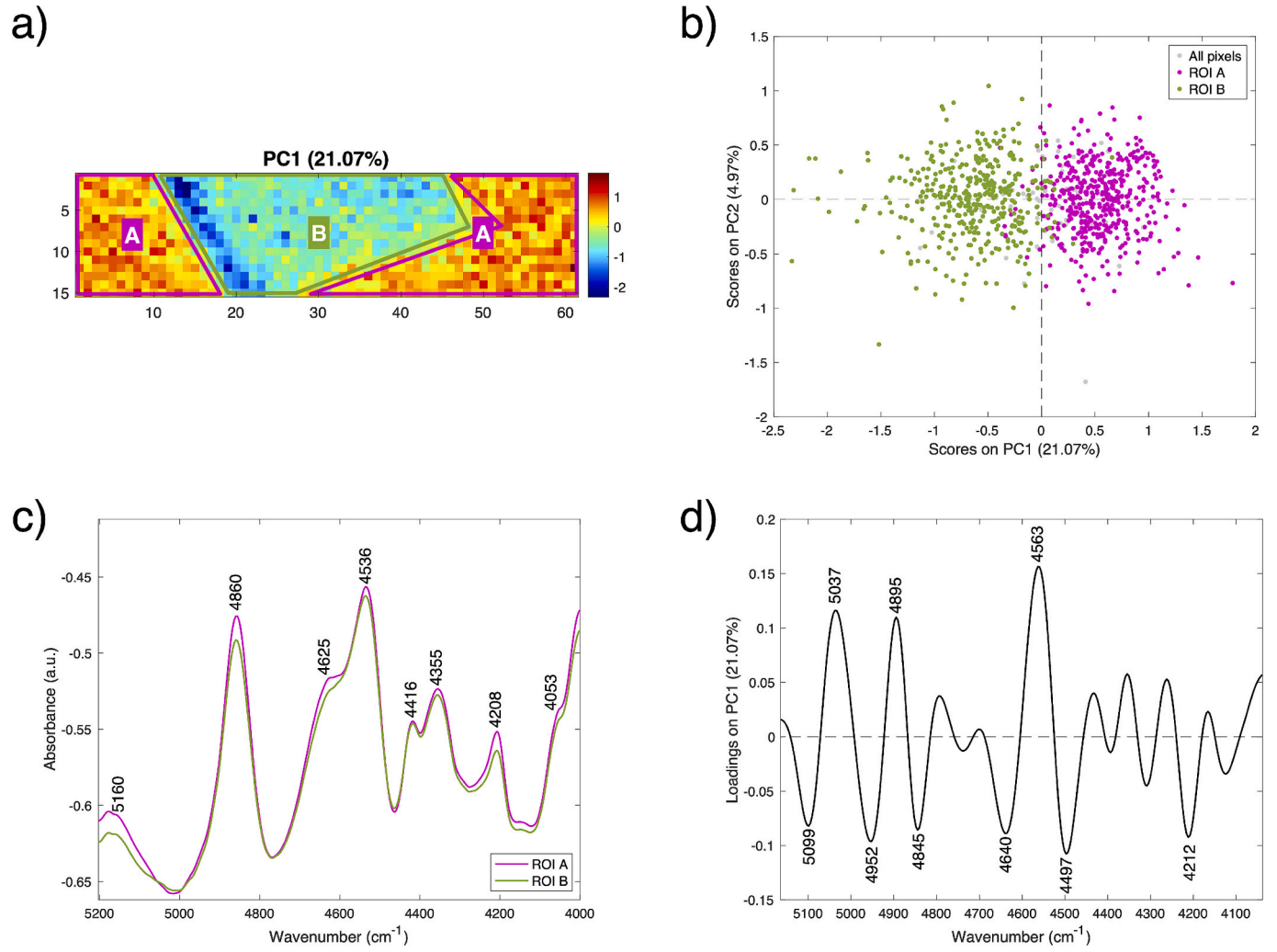

Fig. 4. PCA brushing results of S20 on PC1 score map with a focus on selected NIR region (5200–4000 cm^{-1}). (a) PC1 score map brushing areas; (b) highlighted scores in PCA score plot of two clusters: unirradiated area (A); irradiated area (B); (c) corresponding average spectra with (d) PC1 loading profile from the second derivative PCA model.

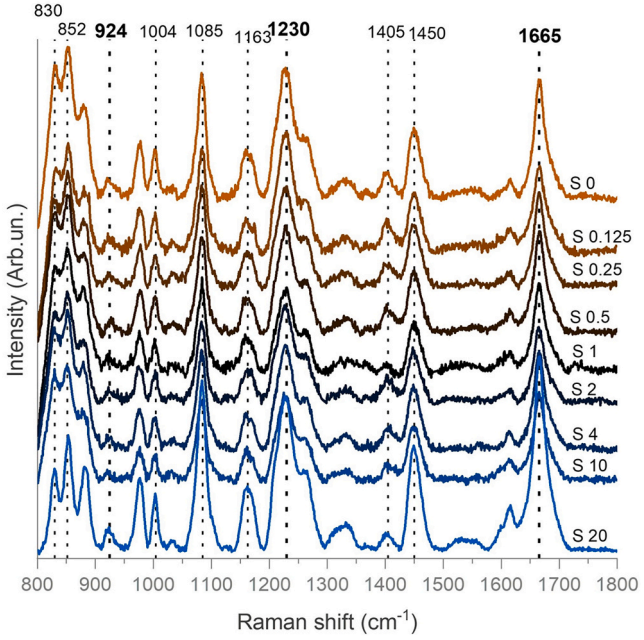

Fig. 5. μ-Raman spectra of proton-irradiated silk samples. Samples are labeled as in Table 1. The effects of the proton beam were analyzed at the penetration depth of ≈ 100 μm.

particular, a decrease in the band intensities at 855 and 830 cm^{-1} was observed in treated samples, indicating degradation or loss of tyrosine. The intensity ratio of this doublet is also sensitive to hydrogen bonding and phenolic hydroxyl ionization: a stronger hydrogen bond is suggested when the 830 cm^{-1} band exceeds that at 855 cm^{-1} [45]. Based on this, and considering that proton beam is expected mainly to affect deeper silk layers, we analyzed the 855/830 cm^{-1} intensity ratios for samples irradiated with 0, 4, 10, and 20 μC/cm^2 measured using a 5× objective, and compared them to virgin silk. As shown in Fig. S21, no significant damage is observed below 10 μC/cm^2. However, slight tyrosine modification appears at 20 μC/cm^2.

4. Conclusion

This paper proposes an anlytical protocol based on the integrated use of NIR-MIR hyperspectral imaging and μ-Raman microscopy to detect early-stage or hidden damage induced by ion beam.

As a proof of concept, we focused on parchment and silk samples treated at different fluences selecting protons accelerated at 1.7 MeV corresponding to a penetration depth of about 50–60 um.

The NIR and MIR results demonstrate the importance of processing the data with chemometric tools to reveal subtle chemical and structural changes that may be invisible to conventional surface-level techniques. For parchment treated with proton energy at 1.73 MeV, spectral features in the MIR range, particularly shifts and broadening in Amide I and II pseudobands, confirmed collagen denaturation at fluences ≥4 μC/cm^2, consistent with hierarchical disruption of collagen fibers under ionizing radiation. Notably, PCA of hyperspectral maps acquired in the NIR range allowed the detection of chemical modifications even at 0.5 μC/cm^2, well below the threshold for visible damage. This is significant, as previous single-point ATR measurements performed on samples treated with higher energy protons failed to detect such early changes (Csepregi et al.; Müller et al.). These results emphasize the ability of NIR spectroscopy to probe subsurface layers and capture degradation processes driven by energy deposition at the Bragg peak.

Micro-Raman spectroscopy enabled the detection of proton beam-induced damage in parchment treated with a dose as low as 0.125 μC/cm^2, suggesting the band at 1087 cm^{-1} as a spectroscopic marker of proton-induced molecular collagen damage. The applied measurement settings allow the detection of changes down to a depth of 100 μm; thus, the entire layer affected by ions in this experiment could be probed.

For silk treated in the same conditions, no visible changes were observed even at the highest dose tested (20 μC/cm^2), indicating a higher resistance to macroscopic damage than parchment. However, PCA applied to both MIR and NIR datasets revealed subtle alterations. While MID spectra allow to identify superficial modifications up to 4 μC/cm^2 and Raman detected a slight tyrosine modification in the sample treated at 20 μC/cm^2, NIR analyses allowed to identify changes up to the samples exposed to 1 μC/cm^2, further supporting the occurrence of internal chemical modifications. Thus, although silk is more stable morphologically, it is still chemically sensitive to irradiation, especially in relation to oxidation pathways.

The distinct behaviour of parchment and silk under proton irradiation, despite both being protein-based, highlights the influence of molecular structure and material morphology on radiation susceptibility. Parchment, primarily composed of cross-linked collagen fibrils, is structurally rigid and more prone to hierarchical degradation. Silk fibroin, by contrast, has a semi-crystalline and less cross-linked architecture, which may confer resilience to structural disruption.

These observations underscore the value of NIR hyperspectral imaging and μ-Raman microscopy to detect incipient or hidden damage in historical materials. Importantly, in parchment samples exposed to intermediate doses, certain features (e.g., cluster C in P20) were only detectable using MIR surface-sensitive data, whereas the NIR signal failed to differentiate them, which suggests that MIR and NIR provide complementary insights into depth-selective damage phenomena. μ-Raman spectroscopy allowed to distinguish subtle effects of lower proton beam irradiation doses in parchment, on the other hand just few modifications were observed in silk, proving that the different setups are complementary.

Future experiments will extend this protocol considering different ion beam conditions in order to define safety thresholds for different kind of materials taking into consideration also variables, such as the state of conservation and the presence of additives in the analyzed objects.

CRediT authorship contribution statement

Mingchi Ma: Writing – original draft, Investigation, Formal analysis. **Zelan Li:** Writing – review & editing, Supervision. **Giorgia Sciutto:** Writing – review & editing, Supervision. **Martina Zangari:** Writing – original draft, Formal analysis. **Tommaso Salzillo:** Writing – review & editing, Supervision. **Elisabetta Venuti:** Writing – review & editing, Supervision. **Zita Szikszai:** Writing – review & editing, Resources. **Boglárka Dönczö:** Writing – review & editing, Resources. **Silvia Prati:** Conceptualization, Funding acquisition, Supervision, Writing – review & editing.

Declaration of competing interest

The authors declare that they have no known competing financial interests or personal relationships that could have appeared to influence the work reported in this paper.

Acknowledgments

We thank the China Scholarship Council program to support Dr. Ma PhD grant (grant ID: 202207820009).

Part of the research has been performed in the frame of the project PE5 CHANGES: Cultural Heritage Active Innovation for Sustainable Society. PE 0000020 CHANGES, - CUP B53C22003780006, PNRR Missione 4 Componente 2 Investimento 1.3, NextGenerationEU.

Appendix A. Supplementary data

Supplementary data to this article can be found online at https://doi.org/10.1016/j.microc.2025.115559.

Data availability

Data will be made available on request.

References

[1] M. Chiari, External beam IBA measurements for cultural heritage, Appl. Sci. 13 (2023) 3366, https://doi.org/10.3390/app13053366.

[2] K. Müller, Z. Szikszai, Á. Csepregi, R. Huszánk, Z. Kertész, I. Reiche, Proton beam irradiation induces invisible modifications under the surface of painted parchment, Sci. Rep. 12 (2022) 113, https://doi.org/10.1038/s41598-021-02993-7.

[3] Á. Csepregi, Z. Szikszai, P. Targowski, M. Sylwestrzak, K. Müller, R. Huszánk, A. Angyal, B. Döncző, Z. Kertész, M. Szarka, I. Reiche, Possible modifications of parchment during ion beam analysis, Herit. Sci. 10 (2022) 140, https://doi.org/10.1186/s40494-022-00781-8.

[4] Derrick M. Evaluation of the State of Degradation of Dead Sea Scroll Samples Using FT-IR Spectroscopy n.d.

[5] S.Z. Szilasi, R. Huszank, D. Szikra, T. Váczi, I. Rajta, I. Nagy, Chemical changes in PMMA as a function of depth due to proton beam irradiation, Mater. Chem. Phys. 130 (2011) 702–707, https://doi.org/10.1016/j.matchemphys.2011.07.048.

[6] S.M. MacDonald, R. Jimenez, P. Paetzold, J. Adams, J. Beatty, T.F. DeLaney, H. Kooy, A.G. Taghian, H.-M. Lu, Proton radiotherapy for chest wall and regional lymphatic radiation; dose comparisons and treatment delivery, Radiat. Oncol. 8 (2013) 71, https://doi.org/10.1186/1748-717X-8-71.

[7] T. Calligaro, V. Gonzalez, L. Pichon, PIXE analysis of historical paintings: is the gain worth the risk? Nucl. Instrum. Methods Phys. Res., Sect. B 363 (2015) 135–143, https://doi.org/10.1016/j.nimb.2015.08.072.

[8] E. Badea, L. Miu, P. Budrugeac, M. Giurginca, A. Mašić, N. Badea, Gatta G. Della, Study of deterioration of historical parchments by various thermal analysis techniques complemented by SEM, FTIR, UV-Vis-NIR and unilateral NMR investigations, J. Therm. Anal. Calorim. 91 (2008) 17–27, https://doi.org/10.1007/s10973-007-8513-x.

[9] E. Mannucci, R. Pastorelli, G. Zerbi, C.E. Bottani, A. Facchini, Recovery of ancient parchment: characterization by vibrational spectroscopy, J. Raman Spectrosc. 31 (2000) 1089–1097, https://doi.org/10.1002/1097-4555(200012)31:12%253C1089::AID-JRS649%253E3.0.CO;2-C.

[10] M. Khalid, T. Bora, A.A. Ghaithi, S. Thukral, J. Dutta, Raman spectroscopy detects changes in bone mineral quality and collagen cross-linkage in Staphylococcus infected human bone, Sci. Rep. 8 (2018) 9417, https://doi.org/10.1038/s41598-018-27752-z.

[11] Y. Ishimaru, Y. Oshima, Y. Imai, T. Iimura, S. Takanezawa, K. Hino, H. Miura, Raman spectroscopic analysis to detect reduced bone quality after sciatic neurectomy in mice, Molecules 23 (2018) 3081, https://doi.org/10.3390/molecules23123081.

[12] F. Cappa, I. Paganoni, C. Carsote, E. Badea, M. Schreiner, Studies on the effects of mixed light-thermal ageing on parchment by vibrational spectroscopy and micro hot table method, Herit. Sci. 8 (2020) 15, https://doi.org/10.1186/s40494-020-0353-z.

[13] M.G. Martinez, A.J. Bullock, S. MacNeil, I.U. Rehman, Characterisation of structural changes in collagen with Raman spectroscopy, Appl. Spectrosc. Rev. 54 (2019) 509–542, https://doi.org/10.1080/05704928.2018.1506799.

[14] G. Reina, S. Orlanducci, E. Tamburri, M.L. Terranova, Nanotechnologies for Cultural Heritage: Nanodiamond for Conservation of Papers and Parchments, Kuala Lumpur, Malaysia, 2014, pp. 93–101, https://doi.org/10.1063/1.4883047.

[15] D. Gao, X. Yang, B. Lyu, L. Xue, Y. Wei, J. Ma, S. Zhou, "Mending with silk" enhances aged silk with mechanical and antibacterial properties, J. Colloid Interface Sci. 680 (2025) 689–698, https://doi.org/10.1016/j.jcis.2024.11.121.

[16] F. Vilaplana, J. Nilsson, D.V.P. Sommer, S. Karlsson, Analytical markers for silk degradation: comparing historic silk and silk artificially aged in different environments, Anal. Bioanal. Chem. 407 (2015) 1433–1449, https://doi.org/10.1007/s00216-014-8361-z.

[17] S. Ling, Z. Qi, D.P. Knight, Z. Shao, X. Chen, FTIR imaging, a useful method for studying the compatibility of silk fibroin-based polymer blends, Polym. Chem. 4 (2013) 5401, https://doi.org/10.1039/c3py00508a.

[18] X. Ben, X. Lu, G. Zhao, Z. Wei, J. Yang, Y. Kan, Internal secondary structural conformational states of silk fibroin studied by Raman spectroscopy with band deconvolution analysis, Biomacromolecules 26 (2025) 1992–2002, https://doi.org/10.1021/acs.biomac.4c01827.

[19] S. Zheng, G. Li, W. Yao, T. Yu, Raman spectroscopic investigation of the denaturation process of silk fibroin, Appl. Spectrosc. 43 (1989) 1269–1272, https://doi.org/10.1366/0003702894203525.

[20] F. Rosi, L. Cartechini, D. Sali, C. Miliani, Recent trends in the application of Fourier Transform Infrared (FT-IR) spectroscopy in Heritage Science: from micro- to non-invasive FT-IR, Phys. Sci. Rev. (2019) 4, https://doi.org/10.1515/psr-2018-0006.

[21] D. Badillo-Sanchez, D. Chelazzi, R. Giorgi, A. Cincinelli, P. Baglioni, Understanding the structural degradation of South American historical silk: a Focal Plane Array (FPA) FTIR and multivariate analysis, Sci. Rep. 9 (2019) 17239, https://doi.org/10.1038/s41598-019-53763-5.

[22] M.V. Padalkar, N. Pleshko, Wavelength-dependent penetration depth of near infrared radiation into cartilage, Analyst 140 (2015) 2093–2100, https://doi.org/10.1039/C4AN01987C.

[23] E. Catelli, Z. Li, G. Sciutto, P. Oliveri, S. Prati, M. Occhipinti, A. Tocchio, R. Alberti, T. Frizzi, C. Malegori, R. Mazzeo, Towards the non-destructive analysis of multilayered samples: a novel XRF-VNIR-SWIR hyperspectral imaging system combined with multiblock data processing, Anal. Chim. Acta 1239 (2023) 340710, https://doi.org/10.1016/j.aca.2022.340710.

[24] J.M. Chalmers, P.R. Griffiths (Eds.), Handbook of Vibrational Spectroscopy, John Wiley & Sons Ltd., Chichester, 2002.

[25] S. Aljboor, A. Angyal, D. Baranyai, E. Papp, M. Szarka, Z. Szikszai, I. Rajta, I. Vajda, Z. Kertész, Light-element sensitive in-air millibeam PIXE setup for fast measurement of atmospheric aerosol samples, J. Anal. At. Spectrom. 38 (2023) 57–65, https://doi.org/10.1039/D2JA00291D.

[26] S. Biri, I.K. Vajda, P. Hajdu, R. Rácz, A. Csík, Z. Kormány, Z. Perduk, F. Kocsis, I. Rajta, The atomki accelerator centre, Eur. Phys. J. Plus 136 (2021) 247, https://doi.org/10.1140/epjp/s13360-021-01219-z.

[27] L. Bertrand, S. Schöder, I. Joosten, S.M. Webb, M. Thoury, T. Calligaro, É. Anheim, A. Simon, Practical advances towards safer analysis of heritage samples and objects, TrAC Trends Anal. Chem. 164 (2023) 117078, https://doi.org/10.1016/j.trac.2023.117078.

[28] T. Calligaro, J.-C. Dran, J. Salomon, Chapter 5 Ion Beam Microanalysis. Comprehensive Analytical Chemistry vol. 42, Elsevier, 2004, pp. 227–276, https://doi.org/10.1016/S0166-526X(04)80009-6.

[29] R.J. Barnes, M.S. Dhanoa, S.J. Lister, Standard normal variate transformation and de-trending of near-infrared diffuse reflectance spectra, Appl. Spectrosc. 43 (1989) 772–777, https://doi.org/10.1366/0003702894202201.

[30] Å. Rinnan, F.V.D. Berg, S.B. Engelsen, Review of the most common pre-processing techniques for near-infrared spectra, TrAC Trends Anal. Chem. 28 (2009) 1201–1222, https://doi.org/10.1016/j.trac.2009.07.007.

[31] J. Trygg, J. Gabrielsson, T. Lundstedt, Background Estimation, Denoising, and Preprocessing. Comprehensive Chemometrics, Elsevier, 2009, pp. 1–8, https://doi.org/10.1016/B978-044452701-1.00097-1.

[32] D.F. Thekkudan, S.C. Rutan, Denoising and Signal-to-Noise Ratio Enhancement: Classical Filtering, Comprehensive Chemometrics, Elsevier, 2009, pp. 143–155, https://doi.org/10.1016/B978-0-444-64165-6.02002-4.

[33] Li-Chan ECY, Introduction to Vibrational Spectroscopy in Food Science, in: J. M. Chalmers, P.R. Griffiths (Eds.), Handbook of Vibrational Spectroscopy, first ed., Wiley, 2001 https://doi.org/10.1002/0470027320.s8934.

[34] J.F. Ziegler, M.D. Ziegler, J.P. Biersack, SRIM – The stopping and range of ions in matter (2010), Nucl. Instrum. Methods Phys. Res., Sect. B 268 (2010) 1818–1823, https://doi.org/10.1016/j.nimb.2010.02.091.

[35] L. Geminiani, F. Paolo Campione, C. Corti, B. Giussani, G. Gorla, M. Luraschi, S. Recchia, L. Rampazzi, Non-invasive identification of historical textiles and leather by means of external reflection FTIR spectroscopy, Spectrochim. Acta A: Mol. Biomol. Spectrosc. 326 (2025) 125184, https://doi.org/10.1016/j.saa.2024.125184.

[36] F. Rosi, A. Daveri, C. Miliani, G. Verri, P. Benedetti, F. Piqué, B.G. Brunetti, A. Sgamellotti, Non-invasive identification of organic materials in wall paintings by fiber optic reflectance infrared spectroscopy: a statistical multivariate approach, Anal. Bioanal. Chem. 395 (2009) 2097–2106, https://doi.org/10.1007/s00216-009-3108-y.

[37] M. Vagnini, C. Miliani, L. Cartechini, P. Rocchi, B.G. Brunetti, A. Sgamellotti, FT-NIR spectroscopy for non-invasive identification of natural polymers and resins in easel paintings, Anal. Bioanal. Chem. 395 (2009) 2107–2118, https://doi.org/10.1007/s00216-009-3145-6.

[38] P. Ricciardi, J.K. Delaney, M. Facini, J.G. Zeibel, M. Picollo, S. Lomax, M. Loew, Near infrared reflectance imaging spectroscopy to map paint binders in situ on illuminated manuscripts, Angew. Chem. 124 (2012) 5705–5708, https://doi.org/10.1002/ange.201200840.

[39] V. Brookes, The Study of Deformation Behaviour and Structure Analysis of Natural Protein Fibres by Raman Spectroscopy, ProQuest Dissertations & Theses, 2005.

[40] A. Sadat, I.J. Joye, Peak fitting applied to Fourier transform infrared and Raman spectroscopic analysis of proteins, Appl. Sci. 10 (2020) 5918, https://doi.org/10.3390/app10175918.

[41] N. Kuhar, S. Sil, S. Umapathy, Potential of Raman spectroscopic techniques to study proteins, Spectrochim. Acta A: Mol. Biomol. Spectrosc. 258 (2021) 119712, https://doi.org/10.1016/j.saa.2021.119712.

[42] A.P. Fellows, M.T.L. Casford, P.B. Davies, Spectral analysis and deconvolution of the amide I band of proteins presenting with high-frequency noise and baseline shifts, Appl. Spectrosc. 74 (2020) 597–615, https://doi.org/10.1177/0003702819898536.

[43] A.M. Herrero, Raman spectroscopy for monitoring protein structure in muscle food systems, Crit. Rev. Food Sci. Nutr. 48 (2008) 512–523, https://doi.org/10.1080/10408390701537385.

[44] M.-E. Rousseau, T. Lefèvre, L. Beaulieu, T. Asakura, M. Pézolet, Study of protein conformation and orientation in silkworm and spider silk fibers using Raman microspectroscopy, Biomacromolecules 5 (2004) 2247–2257, https://doi.org/10.1021/bm049717v.

[45] J. Shao, J. Zheng, J. Liu, C. Carr, Fourier transform Raman and Fourier transform infrared spectroscopy studies of silk fibroin, J. Appl. Polym. Sci. 96 (2005) 1999–2004, https://doi.org/10.1002/app.21346.